Research Article | Vol. 25, No. 9 | 1 May 2017 | OPTICS EXPRESS 10536

Optics EXPRESS

High quality factor photonic crystal filter at $k \approx 0$ and its application for refractive index sensing

YONGHAO LIU,[1] SHULING WANG,[1] DEYIN ZHAO,[1] WEIDONG ZHOU,[1,2] AND YUZE SUN[1,3]

[1]*Department of Electrical Engineering, University of Texas at Arlington, Arlington, Texas, 76019, USA*
[2]*wzhou@uta.edu*
[3]*sun@uta.edu*

Abstract: We report here the refractive index (RI) sensing using the singly degenerate high quality factor (Q) modes in photonic crystal slabs (PCS) with the free-space coupled incident beam close to normal incidence. Q values of $3.2\text{x}10^4$ and $1.8\text{x}10^4$ were achieved for the fabricated PCS in air and aqueous solution, respectively. A spectral sensitivity (S) of 94.5 nm/RIU and a detection limit (DL) of $3\text{x}10^{-5}$ RIU were achieved with our device. Such a high-Q cavity for the singly degenerate mode close to normal incidence is very promising to achieve a lower DL for RI sensing.

OCIS codes: (050.5298) Photonic crystals; (350.4238) Nanophotonics and photonic crystals; (130.2790) Guided waves; (280.1415) Biological sensing and sensors.

References and links

1. I. M. White and X. Fan, "On the performance quantification of resonant refractive index sensors," Opt. Express **16**(2), 1020–1028 (2008).
2. X. Fan, I. M. White, S. I. Shopova, H. Zhu, J. D. Suter, and Y. Sun, "Sensitive optical biosensors for unlabeled targets: A review," Anal. Chim. Acta **620**(1-2), 8–26 (2008).
3. F. Vollmer and L. Yang, "Label-free detection with high-Q microcavities: a review of biosensing mechanisms for integrated devices," Nanophotonics **1**(3-4), 267–291 (2012).
4. M. R. Lee and P. M. Fauchet, "Two-dimensional silicon photonic crystal based biosensing platform for protein detection," Opt. Express **15**(8), 4530–4535 (2007).
5. B. Cunningham, B. Lin, J. Qiu, P. Li, J. Pepper, and B. Hugh, "A plastic colorimetric resonant optical biosensor for multiparallel detection of label-free biochemical interactions," Sens. Actuators B Chem. **85**(3), 219–226 (2002).
6. I. D. Block, L. L. Chan, and B. T. Cunningham, "Photonic crystal optical biosensor incorporating structured low-index porous dielectric," Sens. Actuators B Chem. **120**(1), 187–193 (2006).
7. Y. Guo, J. Y. Ye, C. Divin, B. Huang, T. P. Thomas, J. R. Baker, Jr., and T. B. Norris, "Real-time biomolecular binding detection using a sensitive photonic crystal biosensor," Anal. Chem. **82**(12), 5211–5218 (2010).
8. R. Magnusson, D. Wawro, S. Zimmerman, and Y. Ding, "Resonant photonic biosensors with polarization-based multiparametric discrimination in each channel," Sensors (Basel) **11**(2), 1476–1488 (2011).
9. L. L. Chan, S. L. Gosangari, K. L. Watkin, and B. T. Cunningham, "Label-free imaging of cancer cells using photonic crystal biosensors and application to cytotoxicity screening of a natural compound library," Sens. Actuators B Chem. **132**(2), 418–425 (2008).
10. Y. Sun and X. Fan, "Analysis of ring resonators for chemical vapor sensor development," Opt. Express **16**(14), 10254–10268 (2008).
11. Y. Sun, S. I. Shopova, G. Frye-Mason, and X. Fan, "Rapid chemical-vapor sensing using optofluidic ring resonators," Opt. Lett. **33**(8), 788–790 (2008).
12. W.-C. Lai, S. Chakravarty, X. Wang, C. Lin, and R. T. Chen, "On-chip methane sensing by near-IR absorption signatures in a photonic crystal slot waveguide," Opt. Lett. **36**(6), 984–986 (2011).
13. M. El Beheiry, V. Liu, S. Fan, and O. Levi, "Sensitivity enhancement in photonic crystal slab biosensors," Opt. Express **18**(22), 22702–22714 (2010).
14. C. Nicolaou, W. T. Lau, R. Gad, H. Akhavan, R. Schilling, and O. Levi, "Enhanced detection limit by dark mode perturbation in 2D photonic crystal slab refractive index sensors," Opt. Express **21**(25), 31698–31712 (2013).
15. S. Wang, Y. Liu, D. Zhao, Y. Shuai, H. Yang, W. Zhou, and Y. Sun, "Optofluidic double-layer Fano resonance photonic crystal slab liquid sensors," in *Conference on Lasers and Electro-Optics* (CLEO) (Optical Society of America, 2015), paper STu1F.6.

#287586 https://doi.org/10.1364/OE.25.010536
Journal © 2017 Received 27 Feb 2017; revised 23 Apr 2017; accepted 24 Apr 2017; published 27 Apr 2017

Optics EXPRESS

16. S. Wang, Y. Liu, D. Zhao, H. Yang, W. Zhou, and Y. Sun, "Optofluidic Fano resonance photonic crystal refractometric sensors," Appl. Phys. Lett. **110**(9), 091105 (2017).
17. W.-C. Lai, S. Chakravarty, Y. Zou, Y. Guo, and R. T. Chen, "Slow light enhanced sensitivity of resonance modes in photonic crystal biosensors," Appl. Phys. Lett. **102**(4), 041111 (2013).
18. C. Kang, C. T. Phare, Y. A. Vlasov, S. Assefa, and S. M. Weiss, "Photonic crystal slab sensor with enhanced surface area," Opt. Express **18**(26), 27930–27937 (2010).
19. D. Dorfner, T. Zabel, T. Hürlimann, N. Hauke, L. Frandsen, U. Rant, G. Abstreiter, and J. Finley, "Photonic crystal nanostructures for optical biosensing applications," Biosens. Bioelectron. **24**(12), 3688–3692 (2009).
20. M. G. Scullion, A. Di Falco, and T. F. Krauss, "Slotted photonic crystal cavities with integrated microfluidics for biosensing applications," Biosens. Bioelectron. **27**(1), 101–105 (2011).
21. D. Yang, S. Kita, F. Liang, C. Wang, H. Tian, Y. Ji, M. Lončar, and Q. Quan, "High sensitivity and high Q-factor nanoslotted parallel quadrabeam photonic crystal cavity for real-time and label-free sensing," Appl. Phys. Lett. **105**(6), 063118 (2014).
22. S. Fan and J. D. Joannopoulos, "Analysis of guided resonances in photonic crystal slabs," Phys. Rev. B **65**(23), 235112 (2002).
23. S. G. Johnson, S. Fan, P. R. Villeneuve, J. D. Joannopoulos, and L. A. Kolodziejski, "Guided modes in photonic crystal slabs," Phys. Rev. B **60**(8), 5751–5758 (1999).
24. R. Magnusson and S. S. Wang, "New principle for optical filters," Appl. Phys. Lett. **61**(9), 1022–1024 (1992).
25. W. Zhou, D. Zhao, Y. Shuai, H. Yang, S. Chuwongin, A. Chadha, J.-H. Seo, K. X. Wang, V. Liu, Z. Ma, and S. Fan, "Progress in 2D photonic crystal Fano resonance photonics," Prog. Quantum Electron. **38**(1), 1–74 (2014).
26. Y. Shuai, D. Zhao, A. Singh Chadha, J.-H. Seo, H. Yang, S. Fan, Z. Ma, and W. Zhou, "Coupled double-layer Fano resonance photonic crystal filters with lattice-displacement," Appl. Phys. Lett. **103**(24), 241106 (2013).
27. Y. Shuai, D. Zhao, Z. Tian, J.-H. Seo, D. V. Plant, Z. Ma, S. Fan, and W. Zhou, "Double-layer Fano resonance photonic crystal filters," Opt. Express **21**(21), 24582–24589 (2013).
28. W. M. Robertson, G. Arjavalingam, R. D. Meade, K. D. Brommer, A. M. Rappe, and J. D. Joannopoulos, "Measurement of photonic band structure in a two-dimensional periodic dielectric array," Phys. Rev. Lett. **68**(13), 2023–2026 (1992).
29. K. Sakoda, "Symmetry, degeneracy, and uncoupled modes in two-dimensional photonic lattices," Phys. Rev. B Condens. Matter **52**(11), 7982–7986 (1995).
30. O. Kilic, M. Digonnet, G. Kino, and O. Solgaard, "Controlling uncoupled resonances in photonic crystals through breaking the mirror symmetry," Opt. Express **16**(17), 13090–13103 (2008).
31. J. Lee, B. Zhen, S.-L. Chua, W. Qiu, J. D. Joannopoulos, M. Soljačić, and O. Shapira, "Observation and differentiation of unique high-Q optical resonances near zero wave vector in macroscopic photonic crystal slabs," Phys. Rev. Lett. **109**(6), 067401 (2012).
32. V. Liu, M. Povinelli, and S. Fan, "Resonance-enhanced optical forces between coupled photonic crystal slabs," Opt. Express **17**(24), 21897–21909 (2009).
33. V. Liu and S. Fan, "S4: A free electromagnetic solver for layered periodic structures," Comput. Phys. Commun. **183**(10), 2233–2244 (2012).
34. Z. Qiang, H. Yang, L. Chen, H. Pang, Z. Ma, and W. Zhou, "Fano filters based on transferred silicon nanomembranes on plastic substrates," Appl. Phys. Lett. **93**(6), 061106 (2008).
35. G. M. Hale and M. R. Querry, "Optical constants of water in the 200-nm to 200-μm wavelength region," Appl. Opt. **12**(3), 555–563 (1973).
36. V. Lousse, W. Suh, O. Kilic, S. Kim, O. Solgaard, and S. Fan, "Angular and polarization properties of a photonic crystal slab mirror," Opt. Express **12**(8), 1575–1582 (2004).
37. B. Luk'yanchuk, N. I. Zheludev, S. A. Maier, N. J. Halas, P. Nordlander, H. Giessen, and C. T. Chong, "The Fano resonance in plasmonic nanostructures and metamaterials," Nat. Mater. **9**(9), 707–715 (2010).
38. A. F. Oskooi, D. Roundy, M. Ibanescu, P. Bermel, J. D. Joannopoulos, and S. G. Johnson, "Meep: A flexible free-software package for electromagnetic simulations by the FDTD method," Comput. Phys. Commun. **181**(3), 687–702 (2010).
39. K. Sakoda, *Optical Properties of Photonic Crystals* (Springer, 2005).
40. Z. Yu and S. Fan, "Extraordinarily high spectral sensitivity in refractive index sensors using multiple optical modes," Opt. Express **19**(11), 10029–10040 (2011).
41. K. A. Tetz, L. Pang, and Y. Fainman, "High-resolution surface plasmon resonance sensor based on linewidth-optimized nanohole array transmittance," Opt. Lett. **31**(10), 1528–1530 (2006).
42. Y. Nazirizadeh, U. Lemmer, and M. Gerken, "Experimental quality factor determination of guided-mode resonances in photonic crystal slabs," Appl. Phys. Lett. **93**(26), 261110 (2008).
43. N. Huang, L. J. Martínez, and M. L. Povinelli, "Tuning the transmission lineshape of a photonic crystal slab guided-resonance mode by polarization control," Opt. Express **21**(18), 20675–20682 (2013).
44. J.-N. Liu, M. V. Schulmerich, R. Bhargava, and B. T. Cunningham, "Optimally designed narrowband guided-mode resonance reflectance filters for mid-infrared spectroscopy," Opt. Express **19**(24), 24182–24197 (2011).
45. I. Alvarado-Rodriguez and E. Yablonovitch, "Separation of radiation and absorption losses in two-dimensional photonic crystal single defect cavities," J. Appl. Phys. **92**(11), 6399–6402 (2002).
46. T. Xu, M. S. Wheeler, H. E. Ruda, M. Mojahedi, and J. S. Aitchison, "The influence of material absorption on the quality factor of photonic crystal cavities," Opt. Express **17**(10), 8343–8348 (2009).

Optics EXPRESS

1. Introduction

Optical biosensors have wide applications in biomedical research, healthcare, and environmental monitoring and are immune to electromagnetic interference. Optical biosensing technologies can be divided into two categories: fluorescence-based detection and label-free detection. Label-free optical sensing can provide real-time rapid analysis and requires minimal sample preparation without interfering with the function of the biomolecules [1–3]. Label-free sensors could either detect refractive index (RI) change, absorption change or Raman signal induced by the presence of the analyte [2]. RI sensors have been demonstrated in the detection of biochemical molecular interaction [4–8], drug screening [9], and gases [10–12]. RI sensors can detect the RI change of the bulk solution [13–16], polymer RI and thickness change in gas sensing [10, 11], or RI change due to molecule binding near the sensor surface in aqueous solution [4, 7].

Sensor detection limit (*DL*) can fully describe the performance of a sensor, which can be improved by increasing the quality factor (*Q*) or spectral sensitivity (*S*) [1]. Surface plasmon resonance (SPR) sensors suffer from low *Q* due to strong intrinsic absorption in metal, which increases the ambiguity in determining the spectral resonance location in the presence of the spectral noise [1]. Photonic crystal (PC) devices, including localized PC cavities [4, 17–19], slotted PC cavities [20, 21], and defect-free photonic crystal slabs (PCS) [5, 8, 14, 16], are one of the most promising platforms in building ultra-compact and highly sensitive integrated sensor arrays on-chip due to the enhanced light-matter interaction at the sub-micrometer scale. Localized PC cavities can achieve high *Q* values ~10^4 [4, 17–19], but have moderate *S* ~100 nm/RIU due to small optical field overlap with the analyte. Slotted PC cavities can obtain high *S* of 450 to 500 nm/RIU due to larger overlap between the optical mode and the analyte, while the *Q* (typically 10^3 to 10^4) for these designs is highly sensitive to the fabrication imperfections [20, 21]. For both localized and slotted PC cavities, delicate alignment is needed to couple the light from fiber to in-plane waveguide. Additionally, the detection speed is greatly comprised due to the slow mass transport rate for the analytes to diffuse in and out of the confined nanoscale channels or localized cavities. In a previous work [16], we reported a surface-normal free-space coupled optofluidic sensor based on defect-free 2D PCS with *Q* of 2,800 and *S* of 264 nm/RIU and achieved fast detection and simple alignment for light coupling.

Guided resonances in PCS allow easy coupling to externally vertical incident beams under certain conditions [22–25], resulting in interferences in the reflection or transmission spectra of the PCS. The resonant feature could be very sharp, which can be utilized for optical filters [26, 27]. Dark mode, or termed as uncoupled mode, could not be observed in the reflection or transmission spectra due to symmetry mismatch to the incident plane wave radiation [28–30]. These uncoupled modes have infinite lifetime with infinite *Q* factor, and they are non-degenerate in a square lattice PCS [30]. Coupling to these perturbed dark modes is associated with symmetry breaking, either by varying the lattice structure [14, 30] or introducing finite incident angle [22, 31]. Quality factor of 10^4 and *S* of 800 nm/RIU were achieved by coupling light to slightly perturbed dark modes through alternating nanohole sizes [14]. However, the PCS should be suspended, which is more challenging to fabricate and more fragile at the thin membrane region, compared to the non-suspended counterpart. The non-degenerate (or singly degenerate) modes at small incident angle ($\boldsymbol{k} \approx 0$) have higher *Q* compared to the doubly degenerate modes [22, 31, 32], which could be employed to achieve a lower detection limit in the RI sensor.

In this work, we demonstrated, theoretically and experimentally, RI sensing using the high *Q* singly degenerate modes off normal incidence. A *DL* of 3×10^{-5} RIU has been achieved. These singly degenerate modes are uncoupled modes at normal incidence, but can be observed in the optical spectrum and used for sensing when the mirror symmetry is broken due to finite $\boldsymbol{k}$ vector off normal incidence.

Optics EXPRESS

2. Design

The schematic of the device on silicon on insulator (SOI) substrate is shown in Fig. 1(a), in which top Si layer thickness is 246 nm and SiO_2 thickness is 3 μm. The Si PCS has a lattice constant a = 970 nm and a radius r = 83 nm. An incident plane wave beam with wave vector $\boldsymbol{k}$ shines on the PCS in x-z plane at an incident angle θ and gets reflected back. Figure 1(b) shows the top view and cross-sectional view of scanning electron microscope (SEM) images of one fabricated device.

Reflection spectra of the PCS under normal incidence (along the z-direction) or at a small incident angle are simulated with Stanford Stratified Structure Solver (S^4), a frequency domain code based on coupled wave analysis and S-matrix algorithm [33]. The simulation on angle dependent dispersion properties is similar to the one reported earlier [34]. We simulate one unit cell of the PCS immersed in water. The RI of water is taken to be 1.319 at the PCS resonance modes [35]. The reflection spectrum of the PCS is polarization independent at normal incidence because of 90-degree rotational symmetry of the square lattice [36]. Polarization of the incident optical field is defined with respect to the plane of incidence. Transverse electric (TE) polarization has electric field E_y perpendicular to the plane of incidence (x-z plane), and transverse magnetic (TM) polarization has magnetic field H_y perpendicular to the plane of incidence.

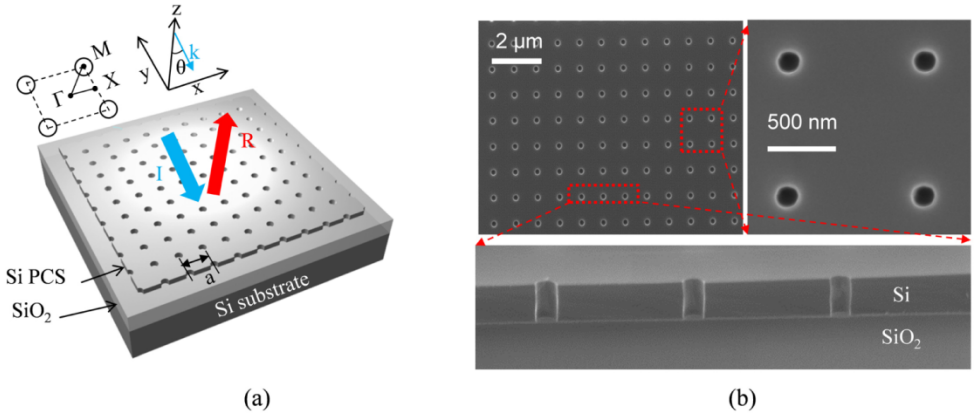

Fig. 1. (a) Schematic of Fano (guided) resonance PCS on SOI substrate. (b) Device SEM top view with zoom in of four holes and angled cross-sectional view of three air holes shown in the inset.

At normal incidence ($\boldsymbol{k}$ = 0, θ = 0°), there exists one doubly degenerate mode at 1530 nm, as shown in black dashed line in Fig. 2(a). At 0.5° incident angle, a new mode A emerges at 1515 nm with TM polarized light source excitation, as shown in Fig. 2(a). The newly emerged non-degenerate mode A is an uncoupled mode at Γ point ($\boldsymbol{k}$ = 0), which has infinite life time and is completely decoupled from the external world [31]. When $\boldsymbol{k}$ is slightly greater than zero, this unique guided resonance has finite lifetime and could couple light in and out of the slab efficiently. At 0.5° incident angle, the singly degenerate mode D could be excited with TE polarized light source. Figure 2(b) shows the dispersion curves of the four energy bands along the Γ-X direction defined in Fig. 1(a) under small incident angles (θ). The doubly degenerate mode at Γ point splits into two modes B and C when incident angle is not zero. The two singly degenerate modes A and D do not continue to $\boldsymbol{k}$ = 0 in Fig. 2(b) because they are uncoupled modes at $\boldsymbol{k}$ = 0.

Optics EXPRESS

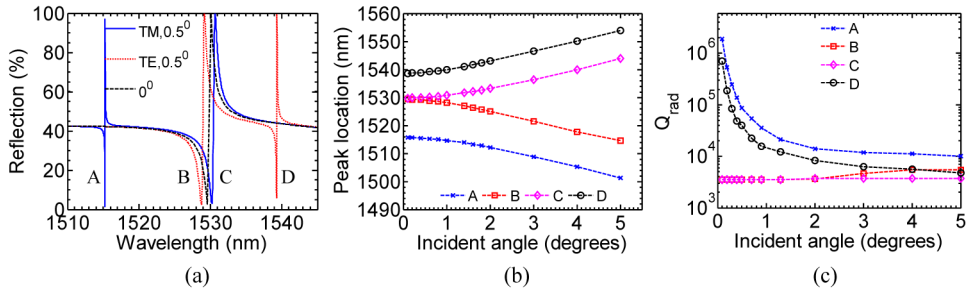

Fig. 2. (a) Simulated reflection spectra for PCS at 0.5 degree and 0 degree incident angles. (b) Simulated band diagram of singly degenerate modes (*A, D*) and doubly degenerate modes (*B, C*) for the PCS. (c) Fano fitted quality factor for reflection spectra at different incident angles for the four modes.

Figure 2(c) depicts the calculated radiative quality factor (Q_{rad}) of these four bands with Fano fitting from simulated reflection spectrum [37]. Bands *B* and *C* originate from the doubly degenerate mode (at Γ point) and they have finite Q_{rad} at $\boldsymbol{k} \approx 0$, the singly degenerate bands *A* and *D* have Q_{rad} that approaches infinity when $\boldsymbol{k} \approx 0$. At Γ point, the doubly degenerate mode has the same symmetry as free-space modes, while the singly degenerate modes *A* and *D* are decoupled from free-space modes due to symmetry mismatch.

In this work, we compared two computational techniques to evaluate the sensor performance of the PCS, including resonance location, sensitivity, quality factor and detection limit. The first technique is S^4, where we simulated spectral sensitivity ($\Delta\lambda/\Delta n_{analyte}$) by tracking guided resonance shift for a unit cell of PCS with different RI of analyte above the PCS. The second technique is MEEP, a freely available finite-difference time-domain (FDTD) implementation [38]. We simulated a unit cell of three-dimensional PCS structures with periodic boundary conditions (PBCs) in plane and perfectly matched layers (PMLs) on top and bottom of the unit cell to absorb outgoing fields. The excitation consists of a broadband planar Gaussian source located above the PCS to solve modes of the PCS. Field distribution for each mode is computed by exciting the PCS with a narrowband planar Gaussian source. In MEEP, resonance frequency and radiative quality factor of each localized mode is calculated with Harminv, a program that decomposes the fields into a sum of sinusoids and determines their frequencies and decay constants.

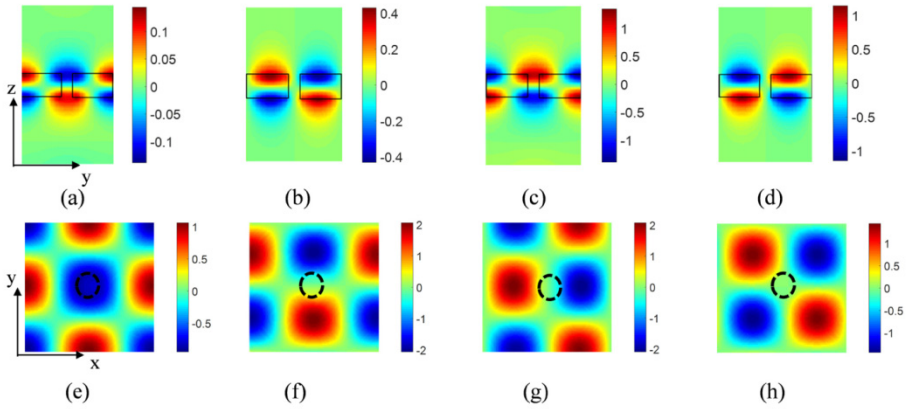

Fig. 3. (a-d) E_x field distribution in *y-z* plane at the center of the hole, (e-h) E_z field distribution in *x-y* plane at the center of PCS for the four modes (a, e) mode *A*, (b, f) mode *B*, (c, g) mode *C*, (d, h) mode *D*, with air hole boundary shown in dashed line and the Si region boundary shown in solid line.

Optics EXPRESS

Figures 3(a)-3(d) shows the E_x component in y-z plane for the four modes excited at 0.5 degree incident angle. These modes have odd symmetry in their electric field with respect to the mirror plane perpendicular to the z axis [13, 23]. The field is greatly extended to the medium above the PCS, which is water in our case. At Γ point, square lattice has a symmetry group of C_{4v} with five irreducible representations. When moving away from Γ point to X point, the symmetry group changes to C_{1h} with only two irreducible representations [39]. The symmetry of each mode could be determined by the mode profile of its E_z component in x-y plane. As shown in Figs. 3(f) and 3(h), Mode B and D are antisymmetric around the x axis, which can be excited by TE polarized source. Figures 3(e) and 3(g) show that mode A and C are symmetric around the x axis and hence can be excited by TM polarized source.

The sensing mechanism in our PCS sensors is the spectral shift of guided resonances due to changes in the RI of the analyte near the PCS top surface. The relation between small change in RI of the surrounding medium and the shift in guided resonance frequency is linear to a first-order approximation based on perturbation theory [40]. We can define optical overlap integral f as the ratio of electric field energy in the analyte region (liquid in our case) to the total energy for a given mode [13, 14].

$$f = \frac{\int_{V_{analyte}} \varepsilon |E|^2 \, dv}{\int_{V_{total}} \varepsilon |E|^2 \, dv} \tag{1}$$

where ε is the dielectric constant of the material. The bulk spectral sensitivity S is related to the optical overlap integral f and the resonance wavelength λ_0 by:

$$S = \frac{\Delta\lambda_0}{\Delta n_{analyte}} = \lambda_0 \frac{f}{n_{analyte}} \tag{2}$$

Therefore it is clear that a large f value will result in a higher bulk sensitivity because of larger field overlap with the analyte. The detection limit describes the smallest RI change that could be measured with a RI sensor [1, 13, 14], which is defined as:

$$DL = \frac{r}{S} \tag{3}$$

where r is the sensor resolution, and r can be taken as three standard deviations (3σ) of the system noise. And σ is related to the signal to noise ratio (SNR) and Q by [1]:

$$\sigma = \frac{\lambda_0}{4.5Q \cdot (SNR)^{0.25}} \tag{4}$$

We also examined the field energy distribution $\varepsilon|E|^2$ for B mode with 0.5 degree incident angle. Figure 4(a) shows the $\varepsilon|E|^2$ distribution in the x-y plane at the center of the PCS (z = −120 nm), with most of the energy confined in the high index silicon region. The $\varepsilon|E|^2$ distribution in the y-z plane at the center of the air hole is plotted in Fig. 4(b). To evaluate how much field energy is concentrated in the liquid region, we plot $\varepsilon|E|^2$ along z axis for the slice of x = 0, as shown with blue solid line in Fig. 4(c). In MEEP, we simulated one unit cell with space resolution of 10 nm, which is sufficient for our structure. We integrated $\varepsilon|E|^2$ along z axis for all the slices at every 10nm from x = - 485 nm to x = 485 nm. The integrated $\varepsilon|E|^2$ is plotted with red solid line in Fig. 4(c). The dashed lines indicate the boundary of PCS, with the PCS-liquid boundary located at z = 0 nm. The optical overlap integral f in the liquid region above the PCS is calculated to be 10.6% by integrating $\varepsilon|E|^2$ for $z > 0$, according to Eq. (1). The f in the air hole of the PCS is around 0.3%, which does not contribute much to the bulk sensitivity. The other three modes A, C and D are also calculated in this way.

Optics EXPRESS

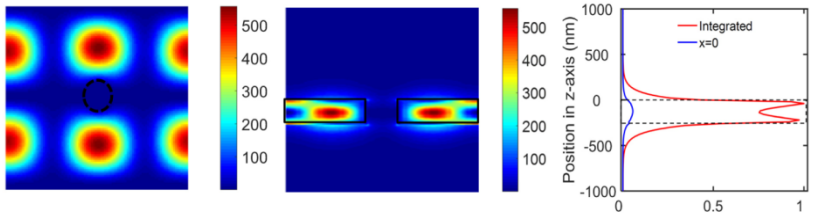

Fig. 4. Simulation of *B* mode at 0.5 degree incident angle. (a) $\varepsilon|E|^2$ profile in *x*-*y* plane at the center of PCS ($z = -120$nm) with air hole boundary shown in dashed line. (b) $\varepsilon|E|^2$ profile in *y*-*z* plane at the center of air hole ($x = 0$), solid lines show the boundary of Si region. (b) Distribution of $\varepsilon|E|^2$ along vertical (*z*-axis) direction for $x = 0$ and integrated $\varepsilon|E|^2$ from –485 nm < x < 485 nm, with dashed lines showing the Si slab boundary.

A summary of the mode properties and sensor performance for the four modes at 0.5 degree incident angle is shown in Table 1. The integrated $\varepsilon|E|^2$ and sensitivity are almost the same for the four modes. For calculation of sensitivity in S^4, we simulated the reflection spectrum for $n_{analyte} = 1.319$ and $n_{analyte} = 1.329$. SNR of 60dB is taken to calculate *DL*. Singly degenerate modes *A* and *D* have one order of magnitude higher *Q* with similar *S* compared with modes *B* and *C*, thereby achieving a lower *DL*.

Table 1. Comparison of resonance location, radiative quality factor, sensitivity, and detection limit of the four modes simulated with S^4 and MEEP.

Computation technique	Modes	*A*	*B*	*C*	*D*
S^4	λ_0 (nm)	1515.3	1529	1530.4	1539.3
	Q_{rad}	86,500	3,500	3,500	39,385
	S (nm/ RIU)	100	105.5	105.4	100.7
	DL (RIU)	4.1×10^{-6}	8.9×10^{-5}	8.9×10^{-5}	8.3×10^{-6}
MEEP	λ_0 (nm)	1518.1	1529.2	1530.2	1538.3
	Q_{rad}	73,772	4,230	4,093	59,582
	f	10.8%	10.9%	10.9%	10.8%
	S (nm/ RIU)	124	126	126	126
	DL (RIU)	3.6×10^{-6}	6.2×10^{-5}	6.4×10^{-5}	4.4×10^{-6}

3. Fabrication and characterization

The PC device was fabricated on SOI substrate with electron beam lithography (EBL) and plasma dry-etching process, with top view SEM and cross sectional view SEM shown in Fig. 1(b). Polydimethylsiloxane (PDMS) microfluidic channel fabricated with soft lithography was bonded on the device after a short oxygen plasma treatment to form the fluidic chamber for aqueous analyte delivery.

Optics EXPRESS

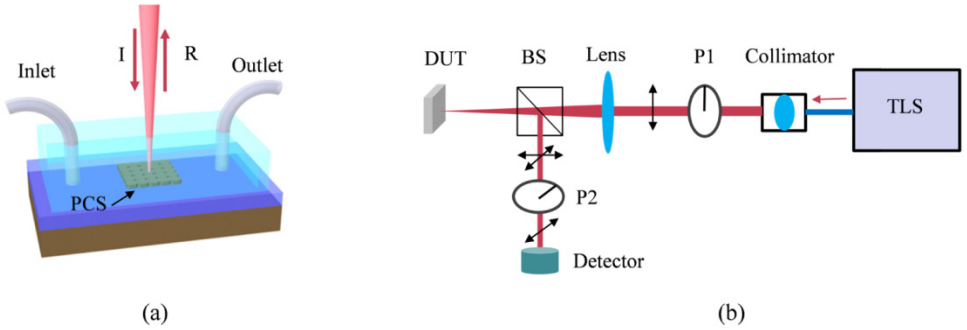

Fig. 5. (a) Schematic of the PCS based optofluidic RI sensor (not to scale). (b) Schematic illustration of the measurement system. TLS: tunable laser source, BS: beam splitter, P1 (P2): polarizer, DUT: device under test.

The schematic of the PCS based optofluidic RI sensor is shown in Fig. 5(a). PDMS thickness is around 2 mm and has negligible optical absorption at PCS resonance wavelength region. Incident light beam passes through the PDMS chamber and shines on the PCS sensor. The test setup is shown in Fig. 5(b). A tunable laser light source (1465~1572 nm, Agilent 81980A) is used and the beam is collimated, polarized and focused onto the 500 x 500 μm^2 PCS device. The reflected light is crossed-polarized in 90 degrees with respect to the incident beam and is collected by a detector. The PCS device is mounted on a translation (*x*-*y*-*z*) stage and a rotation stage for aligning the laser beam to the PCS under normal incidence. The cross-polarization measurement technique suppresses the incident background light, revealing the guided resonance in the reflection spectrum with high extinction ratio (*ER*) [41, 42].

The black curve in Fig. 6(a) shows the tested reflection spectrum of the PCS in air under normal incidence without the use of the cross-polarization technique (i.e. polarizer P2 is removed during the test). Simulated reflection spectrum of the PCS in air is shown as blue dashed line, which matches well with the tested spectrum. When the PCS is immersed in water, the simulated reflection spectrum, shown as red dashed line, indicates around 30 nm red shift compared to the spectrum in air. The Fano resonance is asymmetric lineshape in the reflection spectrum [25]. The quality factor of the measured reflection spectrum is fitted to be 2,690, as shown in Fig. 6(b).

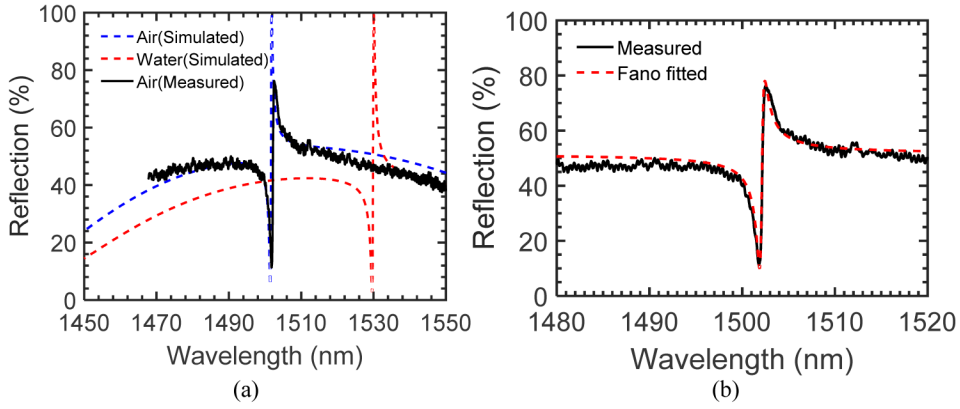

Fig. 6. (a) Simulated reflection spectra of PCS at normal incidence in air and in water and measured reflection spectrum for PCS in air without polarizer. (b) Measured reflection spectrum in air and Fano fitting shows $Q = 2{,}690$.

Optics EXPRESS

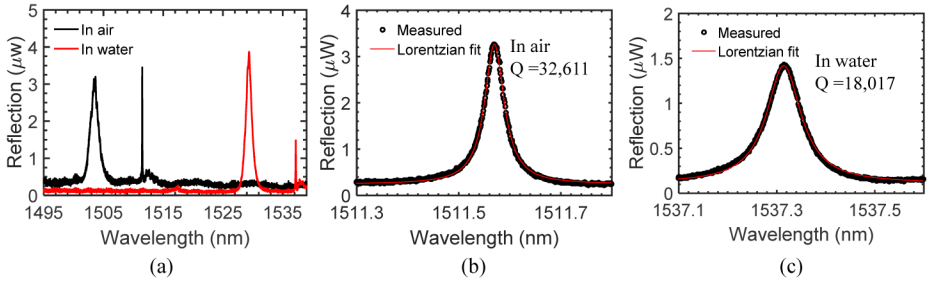

Fig. 7. Measured PCS reflection spectra with cross polarizers in air and in water. (b, c) Lorentzian fit of the measured reflection resonance for *D* mode (b) in air and (c) in water.

The tested reflection spectra of the PCS with cross-polarization technique are shown in Fig. 7(a). The resonances are in Lorentzian lineshape because the Fabry-Perot background light gets suppressed while the guided resonance is revealed [43]. In the test, we had a 10x objective lens to focus the collimated beam with 2 mm waist to 150 μm at the focal plane and the half-angle of divergence for the beam is estimated to be 0.35°. The sample was mounted at the focal plane of the lens, the incoming incident beam includes wave vectors with $\boldsymbol{k} > 0$. Care was taken to align the beam to normal incidence. Two modes *B* and *C* are close to each other on the spectrum when $\boldsymbol{k} \approx 0$ and there is no clear distinction between these two modes. Measured quality factors (Q_M) for the spectrum in air and in water are fitted by Lorentzian fitting [44]. Q_M is $3.2\text{x}10^4$ for the resonance of the PCS tested in air and the Lorentzian fitting is shown in Fig. 7(b). When testing the PCS immersed in water, the resonance spectral linewidth becomes broadened, exhibiting a $Q_M = 1.8\text{x}10^4$, as shown in Fig. 7(c). The extinction ratio is more than 10 dB for these resonances. The measured Q_M can be related to Q_{rad} with the following equation [45].

$$\frac{1}{Q_M} = \frac{1}{Q_{rad}} + \frac{1}{Q_{loss}} \tag{5}$$

where Q_{loss} depends on material absorption and scattering loss due to fabrication imperfection. The reduction of Q_M from $3.2\text{x}10^4$ to $1.8\text{x}10^4$ is due to the absorption of water at this wavelength region [46]. The absorption induced quality factor Q_{abs} is given by [46]:

$$Q_{abs} = n_i / (2fn_r) \tag{6}$$

where n_i and n_r are the imaginary part and real part for the absorptive material, f is the optical overlap integral in the absorptive material. We take n_i as 10^{-4} and n_r as 1.319 [35]. Optical overlap integral f is 10.8% for our structure, as shown in Table 1. Q_{abs} is calculated to be around $6.1\text{x}10^4$, which is the upper bound for the quality factor of PCS sensor in water.

We further characterized the sensing performance of *D* mode with various concentrations of ethanol/deionized (DI) water mixture (0.05% - 0.5% volume ratio). The respective spectra are shown in Fig. 8(a). We performed water rinsing step before injecting new ethanol/DI water mixture to ensure that the PDMS chamber was free of residual ethanol from the previous test run. The resonance peak spectral position at each concentration is found by Lorentzian fitting and the spectral shift is plotted out in Fig. 8(b) with lowest detectable RI change of $3\text{x}10^{-5}$ RIU achieved using 0.05% ethanol/DI water. The bulk sensitivity for mode *D* is fitted to be 94.5 nm/ RIU, which matches well with the simulated sensitivity of 100 nm/ RIU for this mode.

Optics EXPRESS

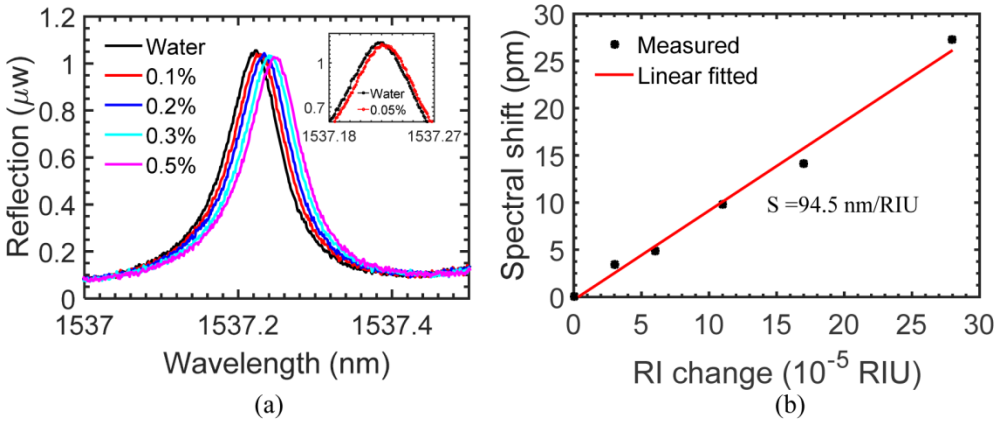

Fig. 8. (a) Measured reflection spectra of the PCS in water and in different concentration of ethanol/DI water mixture, with the spectrum in water and 0.05% ethanol concentration shown in the inset. (b) Bulk sensitivity of the PCS is linear fitted to be 94.5 nm/RIU.

4. Conclusion

We have presented the theoretical background and practical technique to couple light to the singly degenerate modes at $\boldsymbol{k} \approx 0$ which are unobservable under normal incidence due to symmetry mismatch. We discussed the difference between singly degenerate modes and doubly degenerated modes. The high Q values for the singly degenerate modes can lower the detection limit of 2D PCS based RI sensor substantially. High Q value of 10^6 could be achieved theoretically, and high Q of 3.2×10^4 has been achieved in the experiment, which is limited by the angular spreading of the incident beam and fabrication imperfection of the PCS. A DL of 3×10^{-5} RIU was achieved with 94.5 nm/RIU spectral sensitivity.

Funding

US NSF ECCS-1407947 and US ARO W911NF-15-1-0431.